

POLITECNICO
MILANO 1863

ATTITUDE DETERMINATION AND CONTROL OF A 12U CUBESAT

ANNA FONTAN (*945648*)

anna.fontan@mail.polimi.it

SPACECRAFT ATTITUDE DYNAMICS AND CONTROL
Department of Aerospace Engineering
AY 2020 – 2021

Contents

1	INTRODUCTION	3
1.1	Mission description	3
2	ADCS ARCHITECTURE	4
2.1	SENSORS	4
2.1.1	Gyroscope: <i>STIM277H (Sensoror)</i>	4
2.1.2	Earth Horizon Sensor: <i>MAI-SES (Sensoror)</i>	4
2.1.3	Sun Sensor: <i>NFSS-411 (NewSpace)</i>	4
2.2	ACTUATORS	5
2.2.1	Thrusters: <i>SVT01 (Nammo)</i>	5
3	MODEL DESCRIPTION	6
3.1	SPACECRAFT DYNAMICS	6
3.2	ORBITAL MECHANICS	6
3.3	SPACECRAFT KINEMATICS	6
3.4	ENVIRONMENT	6
3.4.1	ATMOSPHERIC DRAG	7
3.4.2	MAGNETIC FIELD	7
3.4.3	GRAVITY GRADIENT	8
3.4.4	SOLAR RADIATION PRESSURE	8
3.5	ACTUATORS	8
3.6	SENSORS	9
3.6.1	GYROSCOPE	9
3.6.2	EARTH HORIZONS AND SUN SENSORS	9
4	CONTROL AND DETERMINATION ALGORITHMS	10
4.1	ATTITUDE DETERMINATION	10
4.2	NOISES FILTERING	10
4.3	DE-TUMBLING	11
4.4	EARTH POINTING MANOEUVRE	11
5	RESULTS	13
5.1	CONTROL-FREE	13
5.2	DE-TUMBLING	13
5.2.1	ANALYSIS OF THE GAIN	13
5.2.2	ATTITUDE AND ANGULAR VELOCITIES	15
5.2.3	CONTROLS	16
5.3	EARTH-POINTING	16
5.3.1	ANALYSIS OF THE GAINS	16
5.3.2	ATTITUDE AND ANGULAR VELOCITIES	17
5.3.3	CONTROLS	18
5.3.4	THRUSTERS ANALYSIS	18
5.3.5	ERRORS	19

Notation

Quantities:			Symbols:	
$\hat{\mathbf{R}}$	Configuration matrix	$[m]$	b	Body frame
ARW	Angular Rate Walk	$[^{\circ}/h]$	CoM	Centre of Mass
\underline{w}	Angular velocity	$[rad/s]$	ECI	Earth-Centered Inertial
A	Area	$[m^2]$	GG	Gravity Gradient
ω	Argument of the perigee	$[deg]$	N	Inertial frame
\mathbf{x}_G	Centre of mass	$[m]$	LEO	Low Earth Orbit
ρ	Density	$[kg/m^3]$	PF	Perifocal
\mathbf{A}_{BN}	Direction cosine matrix	$[-]$	rel	Relative
\underline{d}	Disturbance moment	$[N \cdot m]$	SRP	Solar Radiation Pressure
C_D	Drag coefficient	$[-]$	SC	Spacecraft
e	Eccentricity	$[-]$		
F_e	EM power per unit surface	$[W/m^2]$		
\underline{T}	Force vector	$[N]$		
i	Inclination	$[deg]$		
\underline{u}	Input moment	$[N \cdot m]$		
μ	Gravitation constant	$[km^3/s^2]$		
n	Mean motion	$[rad/s]$		
\mathbf{I}	Moment of Inertia	$[kg \cdot m^2]$		
$\underline{\hat{n}}$	Normal vector	$[-]$		
T	Orbital period	$[s]$		
\underline{r}	Position vector	$[km]$		
\underline{q}	Quaternion vector	$[-]$		
R_{\oplus}	Radius of Earth	$[km]$		
RRW	Rate Random Walk	$[^{\circ}/\sqrt{h}]$		
Ω	Right Ascension of the Ascending Node	$[deg]$		
\mathbf{R}_{313}	Rotational matrix	$[-]$		
T_s	Sampling Time	$[s]$		
p	Semi-latus rectum	$[km]$		
a	Semi-major axis	$[km]$		
$\underline{\hat{S}}$	Sun direction	$[-]$		
\underline{M}	Torque vector	$[N \cdot m]$		
θ	True anomaly	$[deg]$		
\underline{v}	Velocity vector	$[km/s]$		

1 INTRODUCTION

In this report the attitude dynamics and control of a 12U spacecraft in a LEO orbit is analysed. The simulation will account for the presence of several perturbations along with the performance of the ADCS components selected, that will allow Earth pointing throughout the entire mission.

1.1 Mission description

The spacecraft is inserted in an almost circular LEO orbit, which keplerian orbital parameters are reported in Tab. 1.

Table 1: *Keplerian elements of the SC orbit and relative period*

a	e	i	Ω	ω	θ_0	T
6878.1 km	0.0156	10°	0°	0°	0°	1.577 hrs

The shape and configuration of the CubeSat are outlined in Fig. 1a. Hereafter, in Eq. 1, the inertia matrix is expressed alongside the centre of mass.

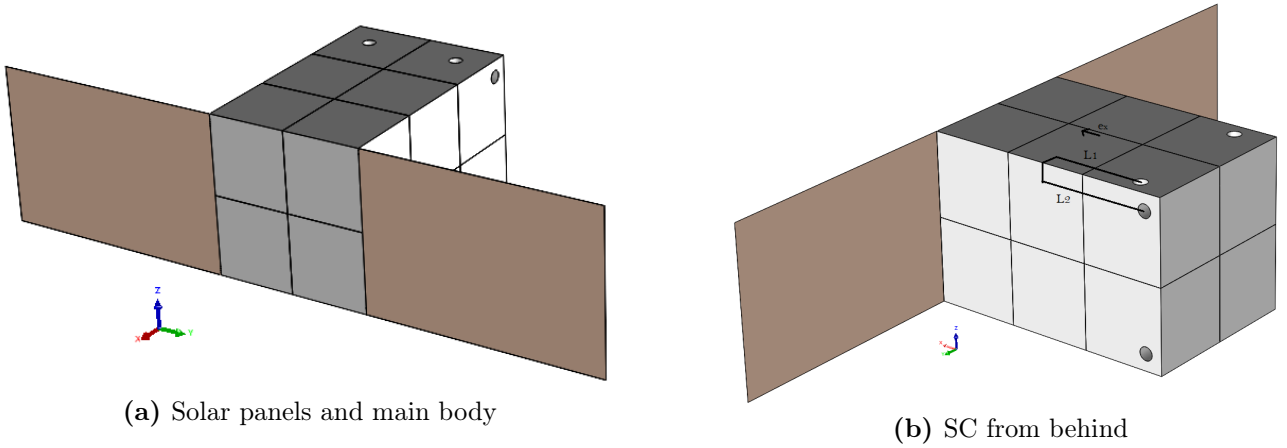


Figure 1: SC configuration (via SOLIDWORKS).

$$\mathbf{I} = \begin{bmatrix} 0.20 & 0 & 0 \\ 0 & 0.23 & 0 \\ 0 & 0 & 0.32 \end{bmatrix} \text{ kg} \cdot \text{m}^2 \quad (1)$$

$$\underline{x}_G = \begin{Bmatrix} 0.02 \\ 0 \\ 0 \end{Bmatrix} m \quad (2)$$

Table 2: *Dimensions and masses of the SC*

	Dimension	Mass
Central body	30 x 20 x 20 cm	15 kg
Solar panel (each)	30 x 20 cm	0.9 kg

2 ADCS ARCHITECTURE

The block scheme of the ADCS architecture is shown in Fig. 2.

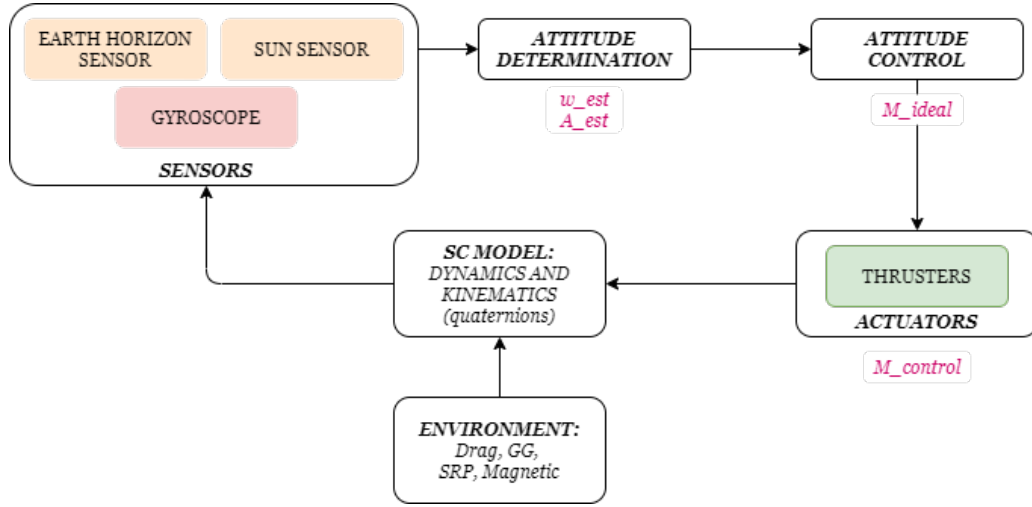


Figure 2: Block scheme of the ADCS architecture

2.1 SENSORS

2.1.1 Gyroscope: *STIM277H (Sensor)*

A gyroscope is added to the configuration, in order to evaluate the angular velocities. In Tab. 3 the specifics are reported.

Table 3: Gyroscope data [1]

ARW	RRW	Sampling Rate	Dimensions	Mass
0.3 °/h	0.15 °/ \sqrt{h}	< 2000 Hz	44.8 x 38.6 x 21.5 mm	52 g

2.1.2 Earth Horizon Sensor: *MAI-SES (Sensor)*

An Earth sensor is added as a first sensor for attitude determination, alongside a Sun Sensor. A typical sampling rate of 1 Hz is considered for lack of more precise information in the datasheet. In Tab. 4 the specifics are reported.

Table 4: Earth Sensor data [2]

Accuracy	Sampling Rate	Field of View	Dimensions	Mass
0.25°	1 Hz	60°	43.3 x 31.8 x 20.7 mm	33 g

2.1.3 Sun Sensor: *NFSS-411 (NewSpace)*

In the end, a Sun Sensor is considered in the system as well, in order to permit to evaluate the attitude. In Tab. 5 the specifics are reported.

Table 5: *Sun Sensor data [3]*

Accuracy	Sampling Rate	Field of View	Dimensions	Mass
$\leq 0.1^\circ$ RMS	5 Hz	140°	34 x 40 x 20 mm	< 35 g

2.2 ACTUATORS

2.2.1 Thrusters: *SVT01 (Nammo)*

For what concerns the actuators, a set of eight cold gas thrusters has been considered to control the attitude of the system. In Tab. 6 the specifics are reported.

Table 6: *Thrusters data [4]*

Valve Response Time	Thrust	Life Cycles	Dimensions	Mass
< 5 ms	10 mN to 100 mN	1,500,000 cycles	16 Ø x 52 mm	60 g

3 MODEL DESCRIPTION

3.1 SPACECRAFT DYNAMICS

The attitude of the spacecraft has been obtained through the integration of the Euler Equations, reported in Eq. 3:

$$\mathbf{I} \dot{\underline{\omega}} = \mathbf{I} \underline{\omega} \wedge \underline{\omega} + \underline{u} + \underline{d} \quad (3)$$

3.2 ORBITAL MECHANICS

In order to describe how the spacecraft position evolves on the orbit only the derivation in time of the true anomaly has been considered, reported hereafter in Eq. 4:

$$\dot{\theta} = \frac{n(1 + e \cos \theta)^2}{(1 - e^2)^{1.5}} \quad (4)$$

Indeed, the perturbations affecting the orbit itself have been neglected for what concerns the keplerian parameters, where the only one that varies is θ .

Moreover, to retrieve the position and velocity vectors in both the Perifocal (Eqs. 5, 7) and ECI (Eqs. 6, 8) reference frames the following equations have been utilised:

$$\underline{r}_{\text{PF}} = r \begin{Bmatrix} \cos \theta \\ \sin \theta \\ 0 \end{Bmatrix} \quad (5)$$

$$\underline{r}_{\text{ECI}} = \mathbf{R}_{313}^T \underline{r}_{\text{PF}} \quad (6)$$

$$\underline{v}_{\text{PF}} = \sqrt{\frac{\mu}{p}} \begin{Bmatrix} -\sin \theta \\ e + \cos \theta \\ 0 \end{Bmatrix} \quad (7)$$

$$\underline{v}_{\text{ECI}} = \mathbf{R}_{313}^T \underline{v}_{\text{PF}} \quad (8)$$

3.3 SPACECRAFT KINEMATICS

In order to describe the kinematics of the spacecraft, the quaternions have been implemented as reported in Eq. 9.

$$\begin{Bmatrix} \dot{q}_1 \\ \dot{q}_2 \\ \dot{q}_3 \\ \dot{q}_4 \end{Bmatrix} = \frac{1}{2} \begin{bmatrix} 0 & \omega_3 & -\omega_2 & \omega_1 \\ -\omega_3 & 0 & \omega_1 & \omega_2 \\ \omega_2 & -\omega_1 & 0 & \omega_3 \\ -\omega_1 & -\omega_2 & -\omega_3 & 0 \end{bmatrix} \begin{Bmatrix} q_1 \\ q_2 \\ q_3 \\ q_4 \end{Bmatrix} \quad (9)$$

Moreover, at each step the result of the integration of the quaternions has been transformed in a unit norm vector. Then the direction cosine matrix has been evaluated as reported in Eq. 10:

$$\mathbf{A}_{\text{BN}} = \begin{bmatrix} q_1^2 - q_2^2 - q_3^2 + q_4^2 & 2(q_1 q_2 + q_3 q_4) & 2(q_1 q_3 - q_2 q_4) \\ 2(q_1 q_2 - q_3 q_4) & -q_1^2 + q_2^2 - q_3^2 + q_4^2 & 2(q_2 q_3 + q_1 q_4) \\ 2(q_1 q_3 + q_2 q_4) & 2(q_2 q_3 - q_1 q_4) & -q_1^2 - q_2^2 + q_3^2 + q_4^2 \end{bmatrix} \quad (10)$$

3.4 ENVIRONMENT

The considered perturbations are related to the atmospheric drag, the magnetic field, the gravity gradient effect and the solar radiation pressure.

Moreover, the atmospheric drag and the magnetic field are the expected to be the most important ones.

3.4.1 ATMOSPHERIC DRAG

The disturbance moment induced by atmospheric drag is computed as the superposition of the contributions given by the surfaces of the spacecraft, as reported in Eq. 12:

$$\begin{cases} \underline{T}_i = -\frac{1}{2}C_D\rho v_{rel}^2 (\hat{n}_i \cdot \hat{v}_{rel}) A_i \hat{v}_{rel} & \text{if } \hat{n}_i \cdot \hat{v}_{rel} > 0 \\ \underline{T}_i = \underline{0} & \text{if } \hat{n}_i \cdot \hat{v}_{rel} \leq 0 \end{cases} \quad (11)$$

$$\underline{M}_{drag} = \sum_i \underline{r}_i \wedge \underline{T}_i \quad (12)$$

where $C_D = 2.2$ and ρ is computed according to the altitude with a function based on an exponential atmospheric model (COSPAR International Reference Atmosphere model CIRA-72). Moreover, \hat{n}_i is the versor normal to the surface, which area is expressed by A_i .

In particular, \underline{v}_{rel} is the relative velocity of the SC with respect to air in the body reference frame and it is obtained as follows:

$$\underline{v}_{rel,N} = \underline{v}_{ECI} - \underline{\omega}_{\oplus} \wedge \underline{r}_N \quad (13)$$

$$\underline{v}_{rel} = \mathbf{A}_{BN} \underline{v}_{rel,N} \quad (14)$$

3.4.2 MAGNETIC FIELD

The perturbation associated to the magnetic field has been modeled as the gradient of a scalar potential V ($\underline{b} = -\nabla V$) and modeled as a series expansion of spherical harmonics, as reported in Eq. 15. The harmonics have been modeled up to order 9:

$$V(r, \theta, \phi) = R \sum_{n=1}^k \left(\frac{R}{r}\right)^{n+1} \sum_{m=0}^n [g_n^m \cos(m\phi) + h_n^m \sin(m\phi)] P_n^m(\theta) \quad (15)$$

where r , θ and ϕ are the spherical coordinates of the position of the satellites, i.e. the distance from the centre of the Earth, the colatitude and East longitude from Greenwich, while g_n^m and h_n^m are the Gaussian coefficients.

Once V is known, the components of the magnetic field can be retrieved as:

$$b_r = -\frac{\partial V}{\partial r} = \sum_{n=1}^k \left(\frac{R}{r}\right)^{n+2} (n+1) \sum_{m=0}^n [g_n^m \cos(m\phi) + h_n^m \sin(m\phi)] P_n^m(\theta) \quad (16)$$

$$b_\theta = -\frac{1}{r} \frac{\partial V}{\partial \theta} = -\sum_{n=1}^k \left(\frac{R}{r}\right)^{n+2} \sum_{m=0}^n [g_n^m \cos(m\phi) + h_n^m \sin(m\phi)] \frac{\partial P_n^m(\theta)}{\partial \theta} \quad (17)$$

$$b_\phi = -\frac{1}{r \sin \theta} \frac{\partial V}{\partial \phi} = -\frac{1}{\sin \theta} \sum_{n=1}^k \left(\frac{R}{r}\right)^{n+2} \sum_{m=0}^n [-g_n^m \sin(m\phi) + h_n^m \cos(m\phi)] P_n^m(\theta) \quad (18)$$

The interaction between Earth's magnetic field and the local magnetic fields on the spacecraft induced by the flow of current induces a torque, which formula is reported in Eq. 19.

$$\underline{M}_{magn} = \underline{m} \wedge \underline{b}_B \quad (19)$$

where the magnetic field in the body frame is given by Eq. 20.

$$\underline{b}_B = \mathbf{A}_{BN} \underline{b}_N \quad (20)$$

Moreover, the parasitic induction is difficult to model in simulation, hence it was assumed as a constant value of $\underline{m} = [0.1, 0.1, 0.1]^T$.

3.4.3 GRAVITY GRADIENT

The disturbance moment of the Gravity Gradient is computed as follows:

$$\underline{M}_{GG} = 3 \frac{\mu}{R_{\oplus}^3} \begin{Bmatrix} (I_z - I_y) c_3 c_2 \\ (I_x - I_z) c_1 c_3 \\ (I_y - I_x) c_1 c_2 \end{Bmatrix} \quad (21)$$

where:

$$\begin{Bmatrix} c_1 \\ c_2 \\ c_3 \end{Bmatrix} = \mathbf{A}_{BL} \cdot \begin{Bmatrix} 1 \\ 0 \\ 0 \end{Bmatrix} \quad (22)$$

3.4.4 SOLAR RADIATION PRESSURE

The sources of electromagnetic radiation that have been considered are the direct solar radiation, the component reflected by Earth and the radiation directly emitted by the planet itself. For the considered altitude, i.e. $h = 700$ km, their values are reported in Tab. 7.

Table 7: Data related to SRP for altitude of 700 km.

Direct solar radiation	Reflected by Earth	Emitted by Earth
1358.00 W/m ²	562.38 W/m ²	135.34 W/m ²

So that the average pressure due to radiation can be evaluated as reported in Eq. 23.

$$F_e = (1358 + 562.38 + 135.34) \frac{W}{m^2} \rightarrow P_e = \frac{F_e}{c} \quad (23)$$

The torque due to SRP is given by Eq. 25, while the resulting force is given by Eq. 24.

$$\begin{cases} \underline{T}_i = -P_e A_i (\hat{\underline{S}}_b \cdot \hat{\underline{n}}_i) \left[(1 - \rho_s) \hat{\underline{S}}_b + \left(2\rho_s (\hat{\underline{S}}_b \cdot \hat{\underline{n}}_i) + \frac{2}{3}\rho_d \right) \hat{\underline{n}}_i \right] & \text{if } \hat{\underline{S}}_b \cdot \hat{\underline{n}}_i^b > 0 \\ \underline{T}_i = \underline{0} & \text{if } \hat{\underline{S}}_b \cdot \hat{\underline{n}}_i^b \leq 0 \end{cases} \quad (24)$$

$$\underline{M}_{SRP} = \sum_i \underline{r}_i \wedge \underline{T}_i \quad (25)$$

In particular, the eclipses were considered as well for the simulation, i.e. when there is no line of sight between the Sun and the SC, according to the model described in [5].

3.5 ACTUATORS

The force vectors and positions of the thrusters from the back of the SC are highlighted in Fig. 3; e_x is the position of the CoM of the SC along the x-axis, l_1 and l_2 are the distances from the CoM along the x-axis.

Knowing the vector of thrusts \underline{F} , the resulting control torque will be given by:

$$\underline{M} = [\hat{\mathbf{R}}] \underline{F} \quad (26)$$

where the configuration matrix $[\hat{\mathbf{R}}]$ is given by Eq. 27.

$$[\hat{\mathbf{R}}] = \begin{bmatrix} -d & d & -d & d & -d & d & -d & d \\ l_1 + e_x & 0 & 0 & -l_1 - e_x & -l_1 - e_x & 0 & 0 & l_1 + e_x \\ 0 & l_2 + e_x & l_2 + e_x & 0 & 0 & -l_2 - e_x & -l_2 - e_x & 0 \end{bmatrix} \quad (27)$$

where $l_1 = 0.11$ m, $l_2 = 0.13$ m, $d = 0.02$ m and $e_x = 0.02$ m.

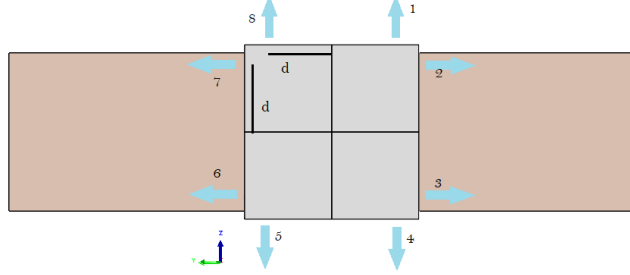


Figure 3: Thrusters.

3.6 SENSORS

In order to retrieve the attitude and the angular velocities, an Earth Horizon, a Sun sensors and a gyroscope have been utilised.

3.6.1 GYROSCOPE

The parameters affecting error related to the gyroscope have been considered accordingly to Tab. 3. Indeed, its output, i.e. the estimation of the velocity vector, is affected by thermo-mechanical (ARW) and electric (RRW) noises; it is simulated as reported in Eq. 28.

$$\underline{\omega}_{gyro} = \underline{\omega} + \underline{n} + \underline{b} \quad (28)$$

where the noises have been modeled as Gaussian (i.e. zero mean):

$$\underline{n} = \sigma_n \underline{\xi}_n \quad (29)$$

$$\underline{b} = \sigma_b \underline{\xi}_b \quad (30)$$

where the variances are derived from bias instability, ARW and T_s as:

$$\sigma_n = ARW \sqrt{T_s} \quad (31)$$

$$\sigma_b = RRW \sqrt{T_s} \quad (32)$$

3.6.2 EARTH HORIZONS AND SUN SENSORS

Given their complexities, the dynamics of the Sun and Earth Horizons sensors have not been simulated, unlikely to the internal dynamics of the gyroscope. Therefore, their output has been considered thus as the true value coming from the dynamics of the system, with additional random noises given by the accuracy of the sensors reported in Tabs. 4 and 5.

For the sensors the position in the body frame of Earth and Sun have been measured as follows in Eqs. 33 and 34.

$$\hat{\underline{s}}_B = \mathbf{A}_\epsilon \mathbf{A}_{BN} \hat{\underline{s}}_N \quad (33)$$

$$\hat{\underline{r}}_B = \mathbf{A}_\epsilon \mathbf{A}_{BN} \hat{\underline{r}}_N \quad (34)$$

4 CONTROL AND DETERMINATION ALGORITHMS

4.1 ATTITUDE DETERMINATION

In order to determine the attitude from the sensors, i.e. the matrix \mathbf{A}_{BN} , SVD algorithm has been implemented. It derives from Whaba's problem that consists in minimising the weight function:

$$J = \frac{1}{2} \sum_{i=1}^N \alpha_i \|\hat{\underline{v}}_{B,i} - \mathbf{A}_{BN} \hat{\underline{v}}_{N,i}\| \quad (35)$$

where $N = 2$ since there are two vector measurements, α_i is the constant that identifies the precision of sensor- i , $\hat{\underline{v}}_{B,i}$ and $\hat{\underline{v}}_{N,i}$ are the unit vectors measured respectively in the body and in the inertial frames. The algorithm follows the procedure hereafter illustrated:

$$\mathbf{B} = \sum_{i=1}^N \alpha_i \hat{\underline{v}}_{B,i} \hat{\underline{v}}_{N,i}^T = \mathbf{U} \mathbf{S} \mathbf{V}^T \quad (36)$$

where \mathbf{U} and \mathbf{V} are orthogonal while \mathbf{S} is a diagonal matrices. Hence:

$$\hat{\mathbf{A}}_{BN} = \mathbf{U} \mathbf{M} \mathbf{V}^T \quad (37)$$

where through MATLAB function *svd* matrices \mathbf{U} and \mathbf{V} can be easily obtained, while:

$$\mathbf{M} = \text{diag}\left[1 \ 1 \ \det(\mathbf{U}) \det(\mathbf{V})\right] \quad (38)$$

4.2 NOISES FILTERING

Both sensors and gyroscope are affected by noises. Hence their outputs, i.e. the angular velocities and the direction cosine matrix, are filtered by the observers in order to have more stable measurements.

For the gyroscope, Eq. 39 has been utilised:

$$\mathbf{I} \dot{\hat{\underline{\omega}}} = \mathbf{I} \hat{\underline{\omega}} \wedge \hat{\underline{\omega}} + \underline{u} + \underline{d} + \alpha_1 (\hat{\underline{\omega}} - \underline{\omega}_{gyro}) \quad (39)$$

while for the sensors instead Eq. 40:

$$\hat{\mathbf{A}}_{BN} = -[\hat{\underline{\omega}}^*] \hat{\mathbf{A}}_{BN} + \alpha_2 (\hat{\mathbf{A}}_{BN} - \mathbf{A}_{BN,sensors}) \quad (40) \quad \hat{\underline{\omega}}^* = \begin{bmatrix} 0 & -\hat{\underline{\omega}}_z & \hat{\underline{\omega}}_y \\ \hat{\underline{\omega}}_z & 0 & -\hat{\underline{\omega}}_x \\ -\hat{\underline{\omega}}_y & \hat{\underline{\omega}}_x & 0 \end{bmatrix} \quad (41)$$

where α_1 and α_2 are tuning parameters (see Tab. 8), $\hat{\mathbf{A}}_{BN}$ and $\hat{\underline{\omega}}$ are the estimations achieved.

Table 8: *Tuning parameters for sensors and gyroscope.*

α_1	α_2
- 0.4	- 0.4

4.3 DE-TUMBLING

In order to proceed with the de-tumble phase, constant thrust jets with an On/Off behaviour have been utilised, which characteristics have been reported in Tab. 6. These permit to reduce the angular velocity to a certain value, close but not identical to zero; once the minimum $||\underline{\omega}||$ is reached, Earth pointing manoeuvre can begin.

The control law in this step is given by Eq. 42, where the ideal control is expressed, proportional to the estimated angular velocity through a gain k (see 9).

$$\underline{u}_{id} = -k \cdot \hat{\underline{\omega}} \quad (42)$$

In order to obtain the control torque, the configuration matrix (see Eq. 27) has been utilised; moreover, the control valve opens only if a certain threshold is reached:

$$\begin{cases} \underline{u}_{real} = [\hat{\mathbf{R}}]^+ \underline{u}_{id} + \gamma \underline{v} \\ \gamma = \max_{i=1,\dots,N} \frac{([\hat{\mathbf{R}}]^+ \underline{u}_{id})_i}{v_i} \\ \underline{v} = [1 \ 1 \ 1 \ 1 \ 1 \ 1 \ 1]^T \end{cases} \quad (43)$$

where $[\hat{\mathbf{R}}]^+$ is the Moore-Penrose pseudoinverse and \underline{v} is the null space vector of \mathbf{R} .

$$\begin{cases} u_{control,i} = F_{\max} & \text{if } \underline{u}_{real,i} \geq \epsilon \\ u_{control,i} = 0 & \text{if } \underline{u}_{real,i} < \epsilon \end{cases} \quad (44)$$

Moreover, a Pulse-Width-Modulator (PWM) has been used as well. Therefore, the time during which the thrusters are on can be computed as follows:

$$\Delta t_{ON} = \frac{u_{ideal,i}}{F_{\max}} \Delta t \quad (45)$$

Once the resulting control force is defined, the respective torque is achieved as follows:

$$\underline{M}_{control} = [\hat{\mathbf{R}}] \cdot \underline{u}_{control} \quad (46)$$

Table 9: *Parameters for De-Tumbling.*

k	ϵ
0.87778	0.01

4.4 EARTH POINTING MANOEUVRE

The aim of this phase is to track a desired time-dependent attitude \mathbf{A}_d while maintaining a desired constant angular velocity $\underline{\omega}_d = \begin{Bmatrix} 0 & 0 & n \end{Bmatrix}^T$.

$$\mathbf{A}_d = \mathbf{A}_{LN} = \begin{bmatrix} \cos(\theta(t)) & \sin(\theta(t)) & 0 \\ -\sin(\theta(t)) & \cos(\theta(t)) & 0 \\ 0 & 0 & 1 \end{bmatrix} \begin{bmatrix} 1 & 0 & 0 \\ 0 & \cos(i) & \sin(i) \\ 0 & -\sin(i) & \cos(i) \end{bmatrix} \quad (47)$$

Knowing these quantities the errors associated to the attitude (Eq. 48) and to the angular velocities (Eq. 49) can be therefore defined:

$$\mathbf{A}_e = \hat{\mathbf{A}} \mathbf{A}_d^T \quad (48)$$

$$\underline{\omega}_e = \underline{\hat{\omega}} - \mathbf{A}_e \underline{\omega}_d \quad (49)$$

Moreover, in this phase a different control law (from the one reported in Section 4.3) is used:

$$\underline{u}_{ideal} = -k_1 \underline{\omega}_e - k_2 [\mathbf{A}_e^T - \mathbf{A}_e]^V + \underline{\hat{\omega}} \wedge \mathbf{I} \underline{\hat{\omega}} + \mathbf{I} (\mathbf{A}_e \dot{\underline{\omega}}_d - \underline{\omega}_e \wedge \mathbf{A}_e \underline{\omega}_d) \quad (50)$$

where the term $\mathbf{A}_e \dot{\underline{\omega}}_d$ does not bring any contribution and the values of the parameters are specified in Tab. 10.

This control has been achieved with variable thrusters. Therefore, the procedure is similar to the one followed for the De-Tumbling, but instead of switching the control to a On/Off state here the actuators open if the thrust is higher than the minimum one:

$$\begin{cases} u_{control,i} = 0 & \text{if } \underline{u}_{real,i} < F_{\min} \\ u_{control,i} = F_{\max} & \text{if } \underline{u}_{real,i} \geq F_{\max} \\ u_{control,i} = [\hat{\mathbf{R}}]^+ u_{id} + \gamma v_i & \text{otherwise} \end{cases} \quad (51)$$

As for the De-Tumbling phase, the response of the valve has been simulated using the *Zero-Order Block*.

Table 10: *Parameters for Earth pointing.*

k_1	k_2
0.4200	0.0164

5 RESULTS

5.1 CONTROL-FREE

For the Control-Free, the initial conditions are:

$$\underline{q}_0 = \begin{Bmatrix} 0 & 0 & 0 & 1 \end{Bmatrix}^T \quad (52)$$

$$\underline{w}_0 = \begin{Bmatrix} 0.8 & 2 & 1 \end{Bmatrix}^T \frac{rad}{s} \quad (53)$$

In this section, the overall evolution of the perturbations affecting the orbit (see Section 3.4) is shown in Fig. 4 for a period of twice two orbits. One can notice indeed the periodicity of the disturbances along the orbit, that vary in time due also to the distance; in particular, starting from the pericentre of the orbit, the drag at the beginning is higher than after half period, when the SC arrives in its apocentre.

Analogously, the eclipses, i.e. when the SC is not in Sun visibility, affect the Solar Radiation Pressure that decreases a lot. Indeed the main contribution given by the Sun is erased and only the ones related to Earth are acting on the SC; however, they are not high enough to appear in the graph.

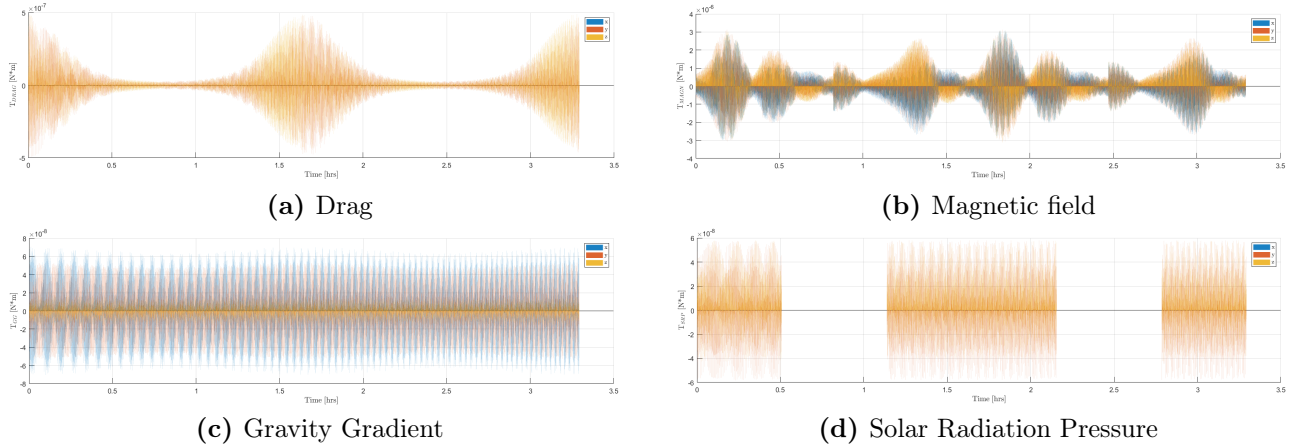


Figure 4: Perturbations for a period of two orbits.

5.2 DE-TUMBLING

The initial parameters of the De-Tumbling phase have been fixed analogously to the Free-Motion phase. Choosing the initial conditions it was noticed that, as expected, the higher the norm of the vector of angular velocities at time t_0 , the longer the time to reach the convergence.

5.2.1 ANALYSIS OF THE GAIN

To decide the value of the gain of the control law (see Section 4.3), k was varied between a minimum value of 0.1 and a maximum of 1.5. Among these, the chosen one has been selected since it leads to the minimum angular velocities, i.e. $\|\underline{\omega}\| \sim 0.001$ rad/s, that is considered for this project sufficiently close to zero to start Earth pointing.

In Fig. 5 the norm of the angular velocity vector for different k is shown.

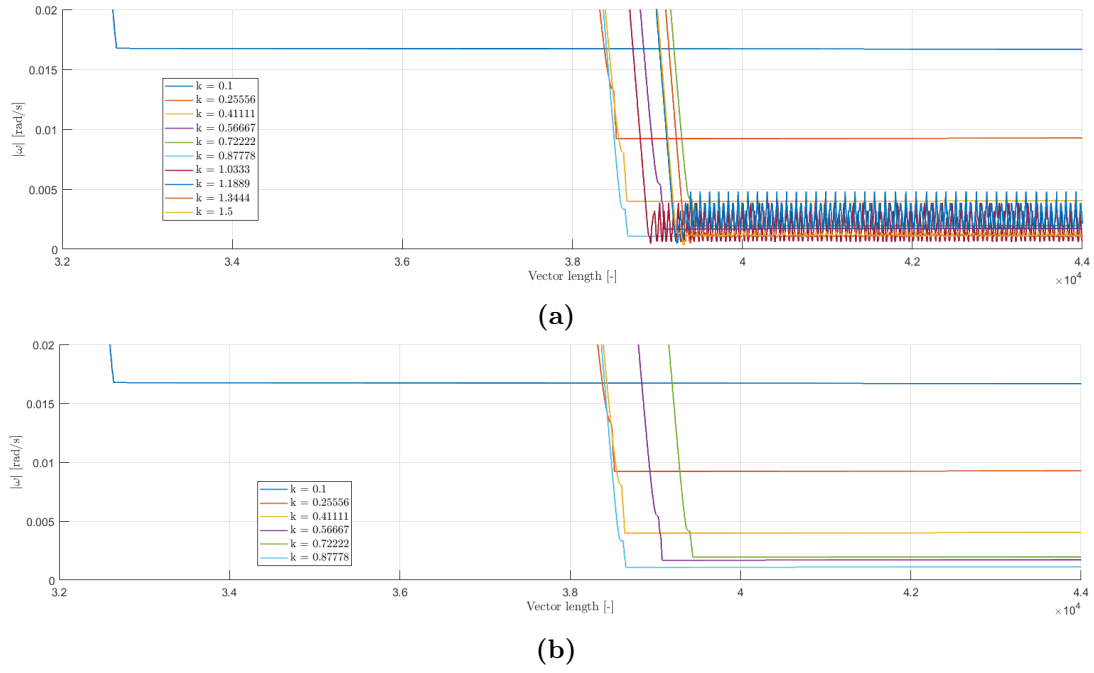


Figure 5: $\|\underline{\omega}\|$ for different gains vs. vector size.

5.2.2 ATTITUDE AND ANGULAR VELOCITIES

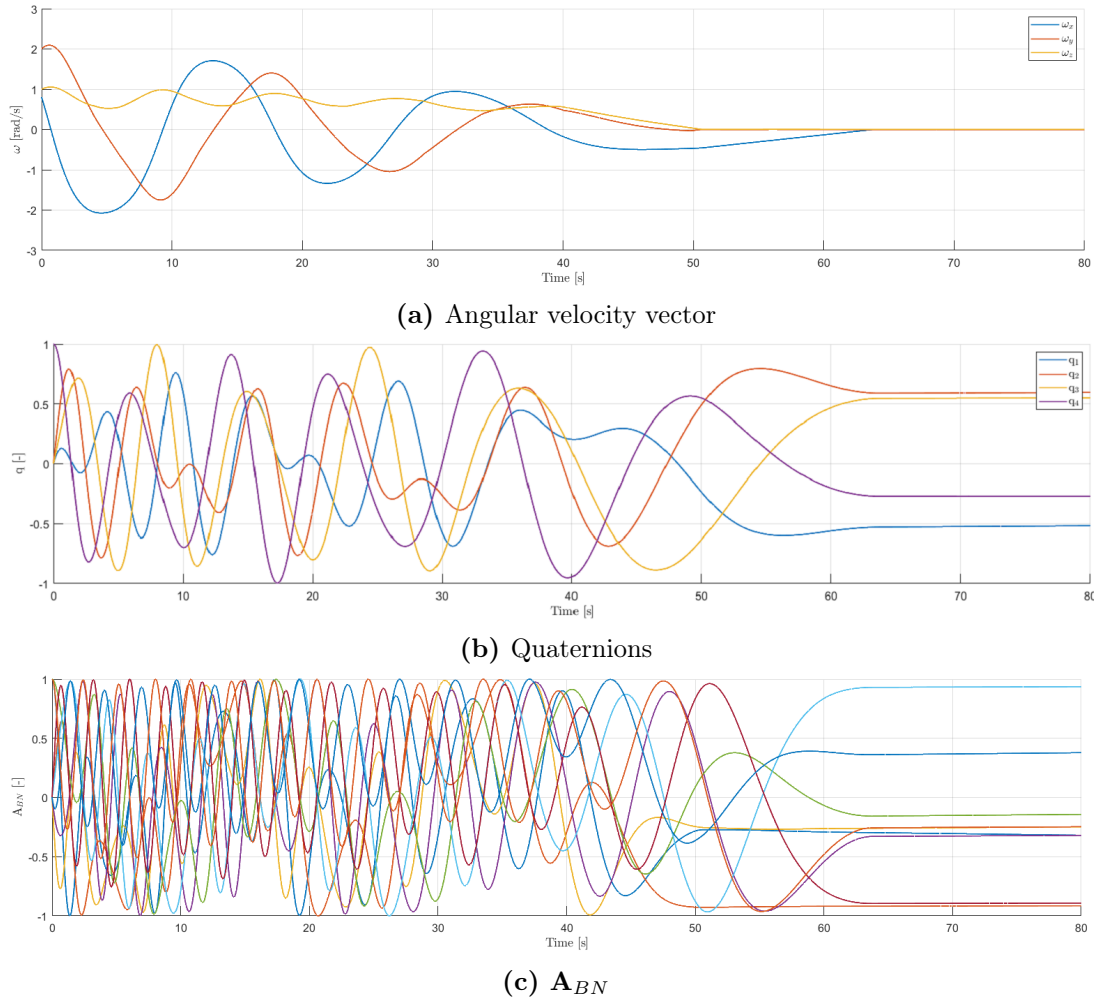


Figure 6: Angular velocities (Fig. 6a), quaternions (Fig. 6b) and Direction Cosine Matrix (Fig. 6c) during the De-Tumbling phase.

From Fig. 6 it can be noticed that the De-Tumbling is completed at ~ 67 s.

5.2.3 CONTROLS

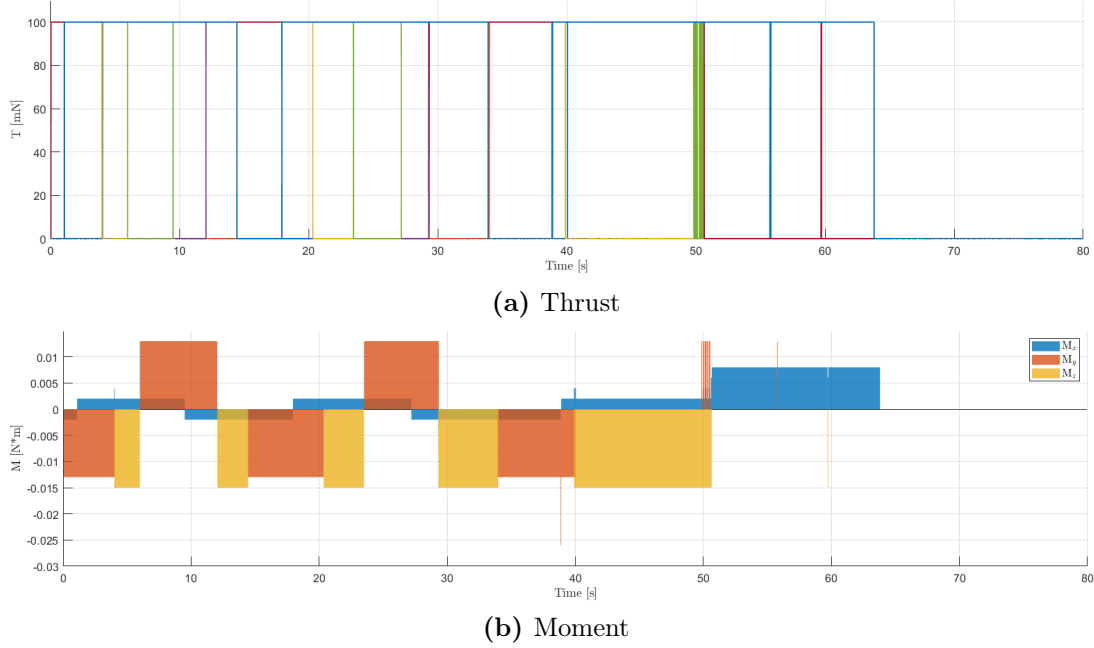


Figure 7: Control force (Fig. 7a) and torque (Fig. 7b) during the De-Tumbling phase.

From Fig. 7 one can notice that some controls are always open, while others for limited times. In particular, the threshold ϵ that has been introduced in the model reduces the chattering problems and also permits to shut down completely all the thrusters once this phase is completed. Moreover, as already specified in the previous sections, this phase is considered concluded even though the SC has not gone exactly to zero: that is due to the presence of disturbances.

5.3 EARTH-POINTING

The initial parameters of the Earth-pointing manoeuvre are given by the final ones of the concluded De-Tumbling phase. Hence:

$$\underline{q}_0 = \begin{Bmatrix} -0.51870 & 0.59099 & 0.55158 & -0.27829 \end{Bmatrix}^T \quad (54)$$

$$\underline{w}_0 = \begin{Bmatrix} -0.10524 & -0.63351 & 0.95285 \end{Bmatrix}^T 10^{-3} \frac{rad}{s} \quad (55)$$

5.3.1 ANALYSIS OF THE GAINS

The two gains that characterise the control law to achieve Earth pointing are k_1 and k_2 . In order to chose them an iterative procedure has been applied, in order to find the best couple that permits to decrease fast and as much as possible the errors.

It was noticed indeed that a higher k_1 leads to longer convergence times, but to a more precise attitude. Instead, as k_2 increases the initial peak of the angular velocities and thrusts increase as well.

Thus, once k_1 has been chosen, the other parameter has been varied accordingly in order to obtain the best result. In Fig. 8 an example is shown, that represents how the maximum peak of the norm of the angular velocities changes with k_2 .

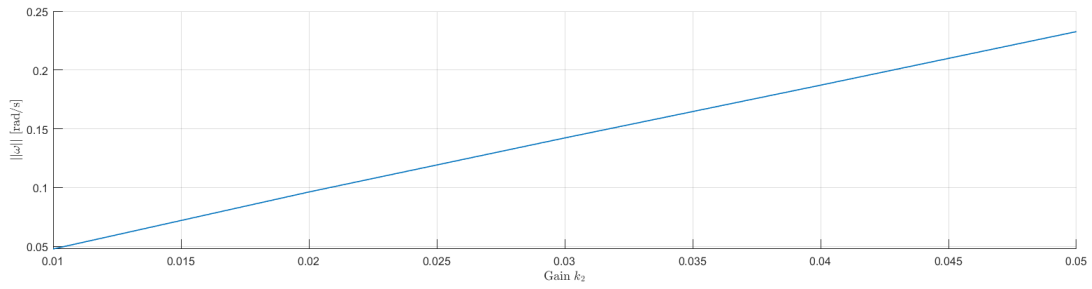
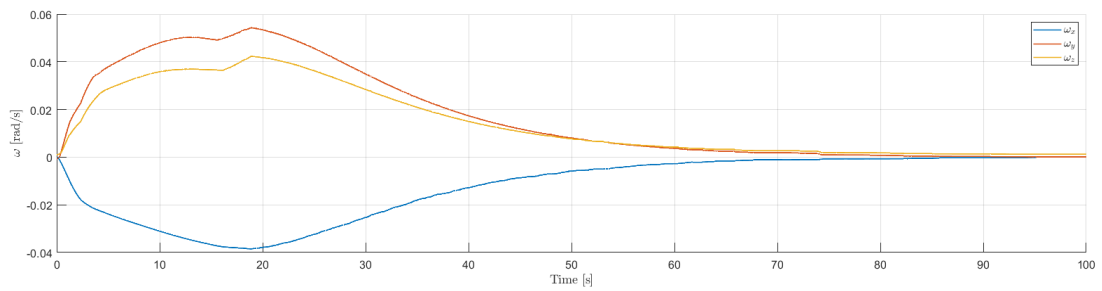
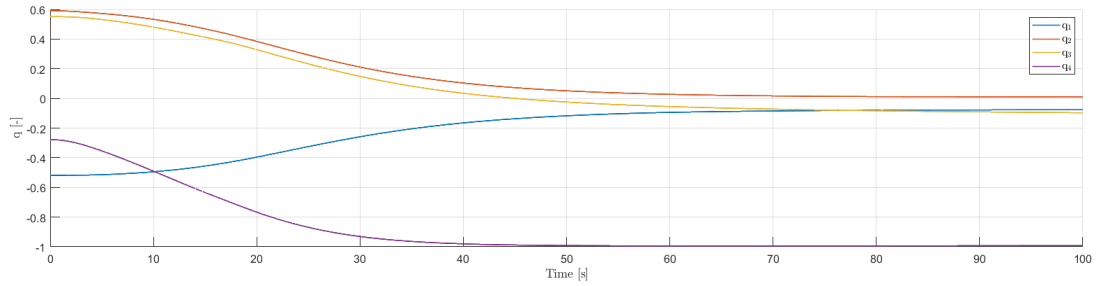


Figure 8: Max of the norm of the angular velocity vector vs gain k_2 .

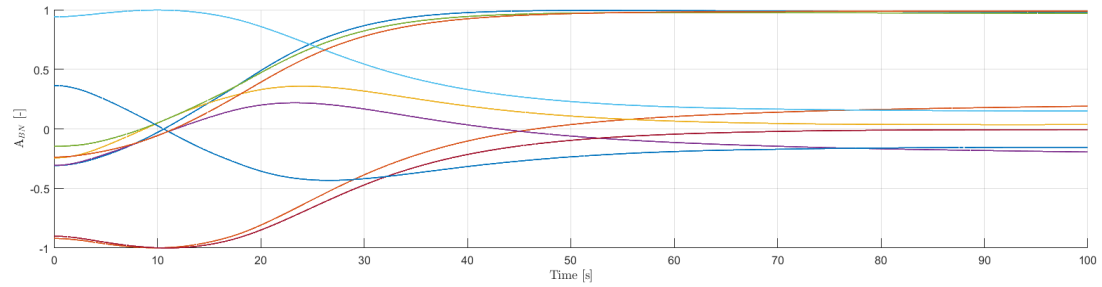
5.3.2 ATTITUDE AND ANGULAR VELOCITIES



(a) Angular velocity vector



(b) Quaternions



(c) A_{BN}

Figure 9: Angular velocities (Fig. 9a), quaternions (Fig. 9b) and Direction Cosine Matrix (Fig. 9c) during Earth pointing.

From Fig. 9 and Fig. 13 it can be noticed that the Earth pointing is completed at ~ 86 s.

5.3.3 CONTROLS

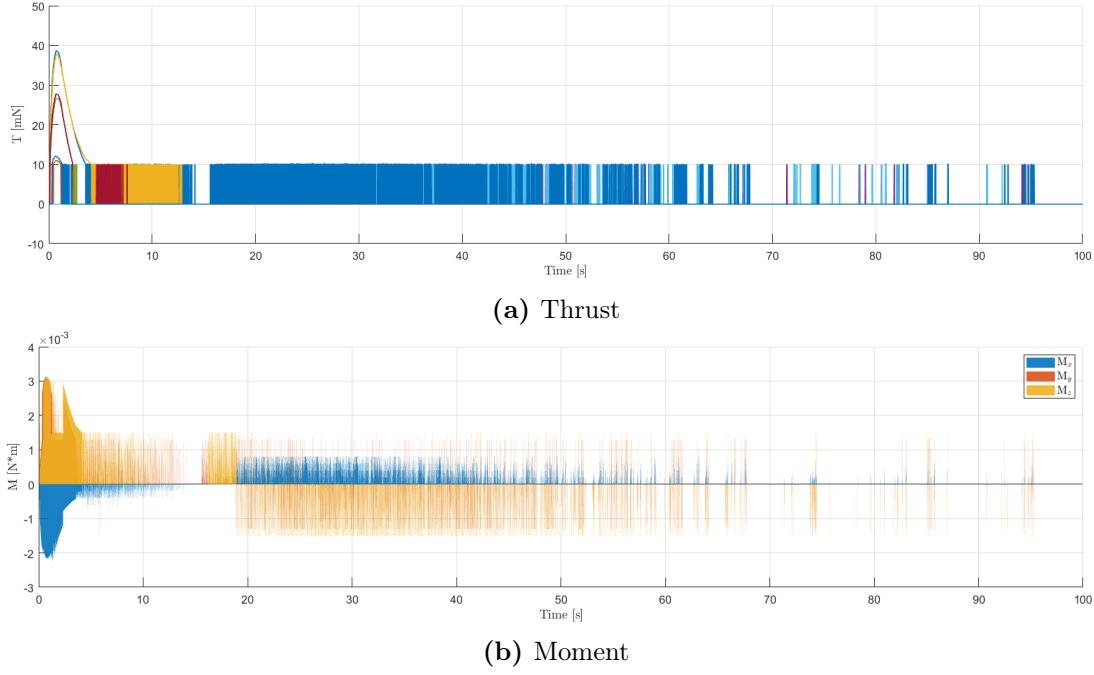


Figure 10: Control force (Fig. 10a) and torque (Fig. 10b) during Earth pointing.

From Fig. 10 one can notice that with respect to the De-Tumbling case, here the maximum thrust is never reached. Moreover, after an initial peak the thrusts have component of the same magnitude ($= F_{\min}$) that permits to bring the errors to almost zero.

5.3.4 THRUSTERS ANALYSIS

An analysis has been conducted over the distances of the thrusters from the CoM. Indeed, the values used in this project have been compared to another couple, $l_1 = 0.01$ m and $l_2 = 0.03$ m, that brings the thrusters much closer to the CoM.

From Fig. 11, as expected, one can notice that the closer the thrusters are to the CoM, the higher the initial peak of the thrusts in order to achieve a good control torque. Instead, for what concerns the pointing accuracy (Fig. 12) there is not an evident difference between the two cases, since they are basically coincident.

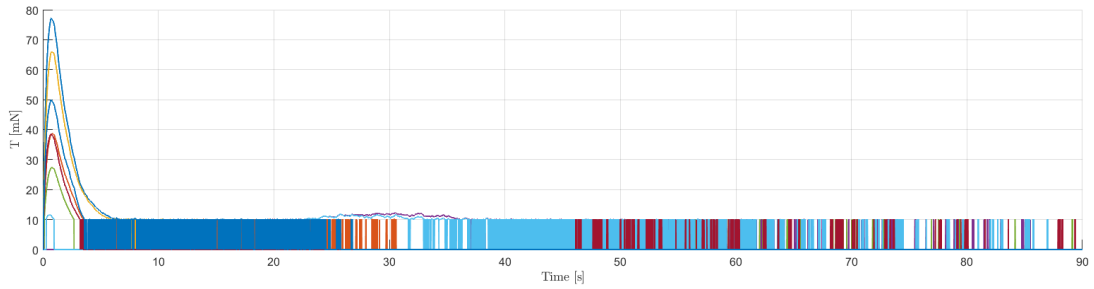


Figure 11: Control thrust for shorter distances of the thrusters from the CoM.

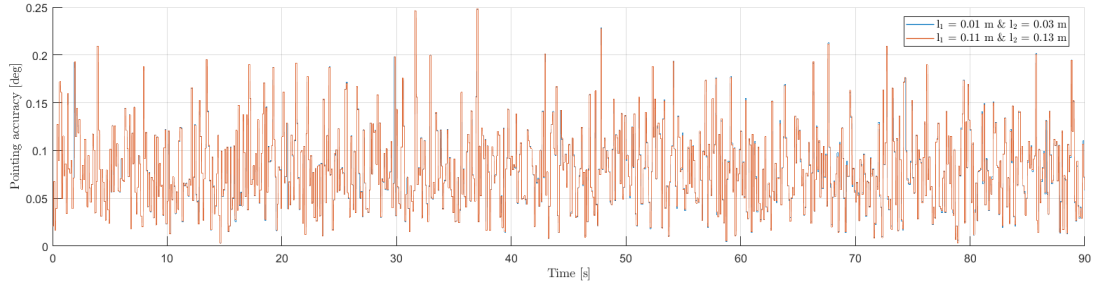


Figure 12: Pointing accuracy for the two cases: Earth Pointing.

5.3.5 ERRORS

The error associated to the Earth pointing are hereafter presented. One can notice that the matrix \mathbf{A}_e tends to the identity one, while in Fig. 13c the difference leads to a null result as expected.

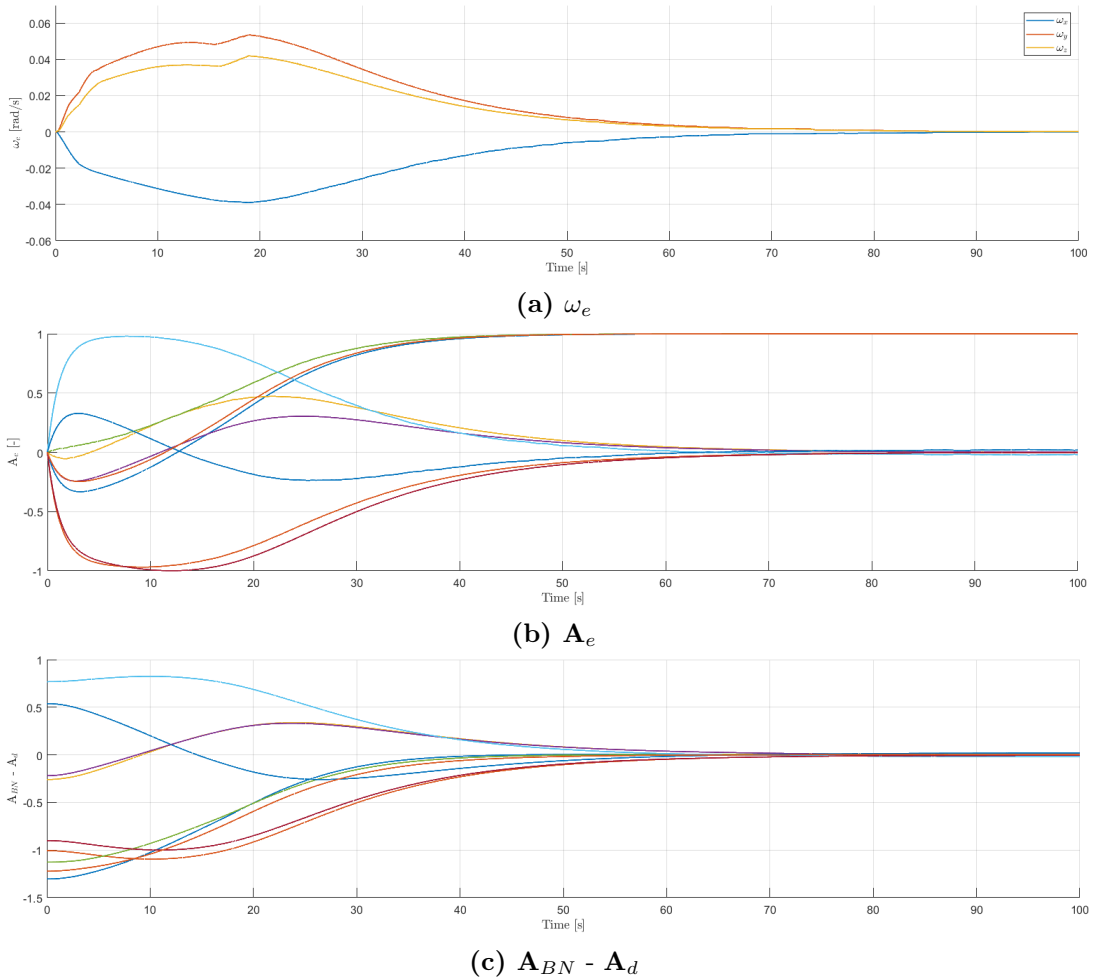


Figure 13: Angular velocities error (Fig. 13a), attitude error (Fig. 13b) and the difference between nominal attitude and desired (Fig. 13c) during Earth pointing.

References

- [1] Sensoror. *STIM277H*. URL: <https://www.sensoror.com/products/gyro-modules/stim277h>.
- [2] Makesat. *Earth Sensor for Satellites*. URL: <https://makesat.com/en/products/earth-sensor-for-satellites>.
- [3] NewSpace SatSearch. *NFSS-411 Sun Sensor*. URL: <https://satsearch.co/products/newspace-systems-nfss-411-fine-sun-sensor>.
- [4] Nammo. *Cold Gas Thruster*. URL: <https://www.nammo.com/product/cold-gas-thruster/>.
- [5] Curtis Howard D. *Orbital Mechanics for Engineering Students*. Elsevier Aerospace Engineering Series. Elsevier, 2014.
- [6] F. B. Zazzera J. D. Biggs. *Lecture Notes*.